

Flame-like Ellerman Bombs and Their Connection to Solar Ultraviolet Bursts

Yajie Chen¹, Hui Tian¹, Hardi Peter², Tanmoy Samanta¹, Vasyl Yurchyshyn³, Haimin Wang^{3,4}, Wenda Cao³, Linghua Wang¹, and Jiansen He¹

School of Earth and Space Sciences, Peking University, Beijing 100871, People's Republic of China; huitian@pku.edu.cn
 Max Planck Institute for Solar System Research, Justus-von-Liebig-Weg 3, D-37077, Göttingen, Germany
 Big Bear Solar Observatory, New Jersey Institute of Technology, 40386 North Shore Lane, Big Bear City, CA 92314-9672, USA
 Center for Solar-Terrestrial Research, New Jersey Institute of Technology, University Heights, Newark, NJ 07102-1982, USA
 Received 2019 March 5; revised 2019 April 7; accepted 2019 April 12; published 2019 April 24

Abstract

Ellerman bombs (EBs) are small-scale intense brightenings in $H\alpha$ wing images, which are generally believed to be signatures of magnetic reconnection around the temperature minimum region of the solar atmosphere. They have a flame-like morphology when observed near the solar limb. Recent observations from the *Interface Region Imaging Spectrograph (IRIS)* reveal another type of small-scale reconnection event called an ultraviolet (UV) burst, in the lower solar atmosphere. Though previous observations have shown a clear coincidence between the occurrence of some UV bursts and EBs, the exact relationship between these two phenomena is still debated. We investigate the spatial and temporal relationship between flame-like EBs and UV bursts using joint near-limb observations between the 1.6 m Goode Solar Telescope (GST) and *IRIS*. In total, 161 EBs have been identified from the GST observations, and \sim 20 of them reveal signatures of UV bursts in the *IRIS* images. Interestingly, we find that these UV bursts have a tendency to appear at the upper parts of their associated flame-like EBs. The intensity variations of most EB-related UV bursts and their corresponding EBs match well. Our results suggest that some of these UV bursts and EBs likely form at different heights during a common reconnection process.

Key words: magnetic reconnection - Sun: chromosphere - Sun: photosphere - Sun: transition region - Sun: UV radiation

1. Introduction

Solar Ellerman bombs (EBs) are characterized as compact intense brightenings in images of the extended H α wings (Ellerman 1917; Ding et al. 1998; Georgoulis et al. 2002; Watanabe et al. 2008, 2011; Nelson et al. 2013, 2015; Vissers et al. 2013, 2015; Yang et al. 2013; Rezaei & Beck 2015). They reveal no obvious signatures in H α core images, and are generally believed to result from magnetic reconnection around the temperature minimum region (TMR). EBs are usually found in active regions (ARs), though recent observations also show similar features in the quiet Sun (Rouppe van der Voort et al. 2016; Nelson et al. 2017). EBs often exhibit a flame-like morphology when observed near the solar limb with highresolution instruments (Hashimoto et al. 2010; Watanabe et al. 2011; Rouppe van der Voort et al. 2016). Recent 3D magnetohydrodynamic (MHD) simulations have reproduced some properties of flame-like EBs (Danilovic 2017; Hansteen et al. 2017).

Ultraviolet (UV) bursts are another type of small-scale reconnection event in the lower solar atmosphere, often observed in emerging ARs (e.g., Peter et al. 2014; Chitta et al. 2017; Zhao et al. 2017; Toriumi et al. 2017; Tian et al. 2018b; Young et al. 2018; Chen et al. 2019) and sunspot light bridges (Toriumi et al. 2015; Tian et al. 2018a). These events refer to intense compact brightenings in transition region (TR) images taken by the *Interface Region Imaging Spectrograph (IRIS*; De Pontieu et al. 2014). They were named "hot explosions" or "*IRIS* bombs" in some earlier studies (e.g., Peter et al. 2014; Tian et al. 2016). The spectral profiles of some emission lines from the Si IV and C II ions in UV bursts are significantly enhanced and broadened, often with several chromospheric absorption lines such as Ni II 1335.20 and 1393.33 Å superimposed.

Coordinated IRIS and ground-based observations show that some EBs are connected to UV bursts (Kim et al. 2015; Vissers et al. 2015; Tian et al. 2016), possibly indicating heating of the plasmas near the TMR to more than 10^4 K (e.g., Rutten 2016). However, 1D radiative transfer models of EBs suggest that the TMR cannot be heated to such high temperatures (Fang et al. 2006, 2017; Bello González et al. 2013; Berlicki & Heinzel 2014; Hong et al. 2014, 2017a, 2017b; Reid et al. 2017). On the other hand, MHD simulations of reconnection show that plasmas around the TMR can be heated to a few tens of thousand Kelvin if the magnetic field is strong and plasma β is low (Ni et al. 2016, 2018a, 2018b). Hansteen et al. (2017) successfully reproduced EBs and UV bursts at different heights in 3D radiative MHD simulations. However, in these simulations EBs and UV bursts occur at different times and different locations, which is different from observations.

The exact relationship between EBs and UV bursts is still debated. The fact that existing EB models cannot produce UV burst signatures possibly implies that these two types of events occur at different heights (e.g., Fang et al. 2017). Due to line-of-sight superposition, the possible height difference is difficult to resolve from disk-center observations. However, near the limb EBs often reveal a flame-like structure due to the projection effect. With such a viewing angle, the possible height difference may be resolved from coordinated observations between *IRIS* and a large-aperture ground-based telescope.

In this Letter, we investigate the spatial and temporal relationship between flame-like EBs and their corresponding UV bursts using coordinated near-limb observations between *IRIS* and the 1.6 m Goode Solar Telescope (GST; Cao et al. 2010). Our results suggest that UV bursts and EBs likely occur at different heights during a common reconnection process.

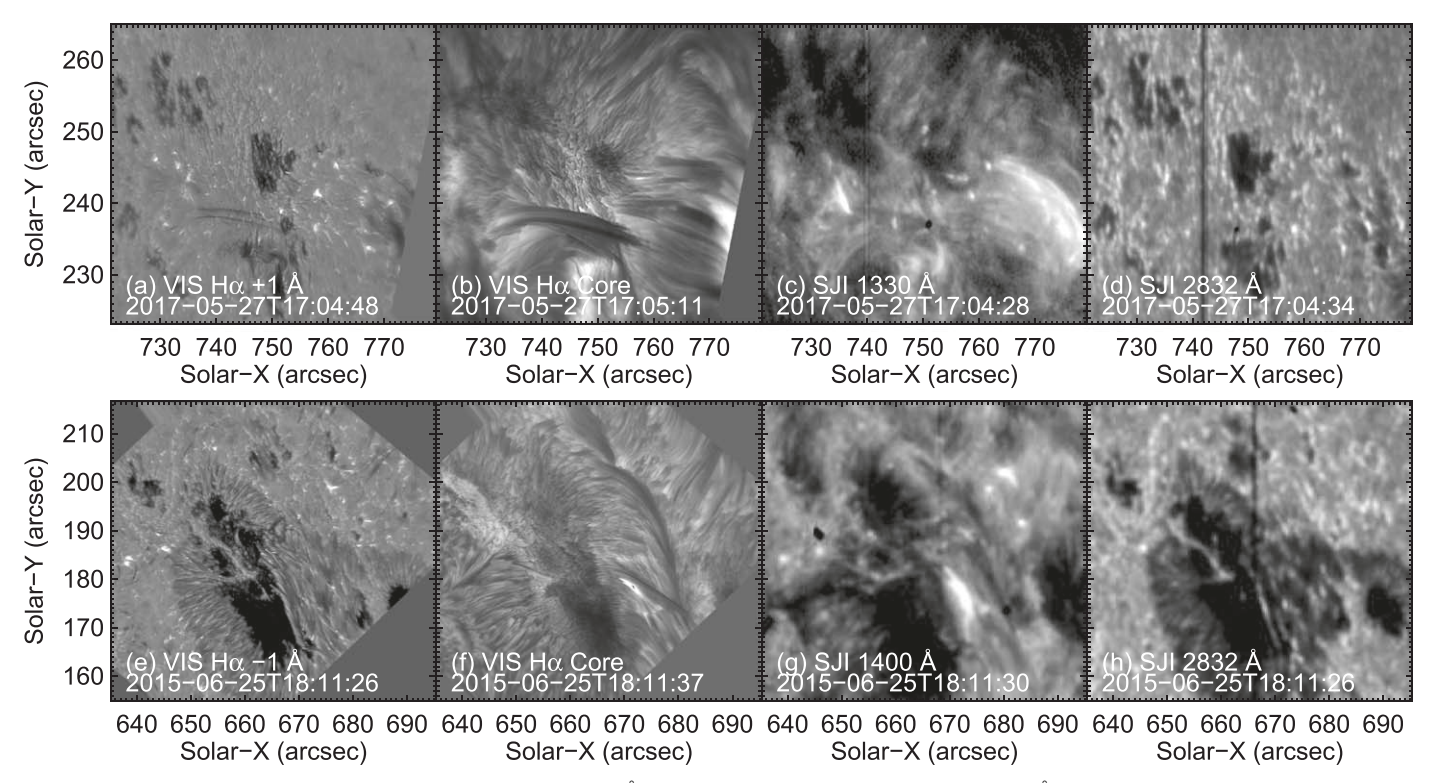


Figure 1. Overview of the two observations. (a)–(d): GST/VIS $H\alpha + 1$ Å and $H\alpha$ core images, *IRIS*/SJI 1330 and 2832 Å images taken around 17:04:48 UT on 2017 May 27. (e)–(f): GST/VIS $H\alpha - 1$ Å and $H\alpha$ core images, *IRIS*/SJI 1400 and 2832 Å images taken around 18:11:26 UT on 2015 June 25. The intensities are shown in arbitrary units.

2. Observations and Data Reduction

We first searched coordinated near-limb observations between GST and *IRIS* satisfying the following criteria: (1) GST took images at H α core and ± 1 Å; (2) *IRIS* took images with the 2832 Å filter and at least one of the 1330/1400 Å filters. Only two data sets meet our criteria.

The first data set was taken on 2017 May 27. IRIS performed a large coarse 16-step raster (120" along the slit, 16 raster steps with a 2" step size) of NOAA AR 12659 during 17:01-22:07 UT. The pointing coordinate was (740", 185"). Slit-jaw images (SJIs) were taken with the 1330, 2796, and 2832 Å filters, at cadences of 21 s, 21 s, and 83 s, respectively. We only used SJI 1330 and 2832 A, and degraded the temporal resolution of the 1330 Å images to that of the 2832 Å images. The spatial pixel size was ~ 0.17 for both SJI and spectral images. The spectral dispersion was $\sim 0.051 \,\text{Å}/\sim 0.025 \,\text{Å}$ in the near/far-ultraviolet band. In this observation images of the Si IV 1393.76 Å spectral window were not transmitted to the ground. The Visible Imaging Spectrometer (VIS) of GST took images at H α core, and H α wings at ± 1 , ± 0.8 , ± 0.6 , ± 0.4 and ± 0.2 Å alternately during 16:43–22:43 UT, with a \sim 53 s cadence at each wavelength position. The spatial pixel size of H α images was $\sim 0'' 03$.

The second data set was obtained on 2015 June 25. *IRIS* performed a large sparse 16-step raster (120" along the slit, 16 raster steps with a 1" step size) of NOAA AR 12371 during 17:22–22:05 UT. The pointing coordinate was (656", 249"). SJIs were taken with all the four filters, each with a cadence of $\sim\!17$ s. Only the 1400 and 2832 Å images were used. We did not use the 1330 Å images, because the same UV bursts are present in both the 1400 and 1330 Å images and UV bursts were identified primarily from the Si IV 1393.76/1402.77 Å

lines in many previous studies. The spatial pixel size was $\sim\!\!0.^{\!\!\prime\prime}\!\!/33$ for SJI images. As the slit did not cross any EB-related UV bursts in this observation, the spectral data were not analyzed. The GST/VIS took images at H α core, and H α wings at ± 1 and ± 0.6 Å alternately during 16:49–21:46 UT. The cadence of H α images at each wavelength was $\sim\!\!34$ s, and the spatial pixel size was $\sim\!\!0.^{\!\!\prime\prime}\!\!03$. We degraded the temporal resolution of SJI images to that of VIS images.

The coalignment procedures between the *IRIS* and GST/VIS images for both data sets are similar: (1) we used the fiducial lines of *IRIS* to coalign the images taken in different SJI filters and spectral windows. (2) The *IRIS* SJI 2832 Å images were internally aligned by using the cross-correlation technique to remove jitters. The obtained shifts were applied to the simultaneously taken 1330/1400 Å and spectral images. (3) After filtering out bad frames, the GST/VIS images taken at each wavelength position were internally aligned using the cross-correlation technique. (4) By comparing commonly observed features such as sunspots and/or fibrils, VIS images taken at different wavelengths can be coaligned. (5) The coalignment between SJI and VIS images was finally achieved by comparing commonly observed features of sunspots and granules in the 2832 Å and H $\alpha \pm 1$ Å images frame by frame.

3. Results and Discussion

Figure 1 presents snapshots of the two observations. For each data set only part of the field of view (FOV) is shown. From the H α ± 1 Å image sequences, some compact brightenings can be identified around the sunspots. We used a criterion of 5σ above the mean intensity at +1 Å over the whole FOV to select EB candidates in the 2017 May 27 data. For the 2015 June 25 observation we used the -1 Å images, as

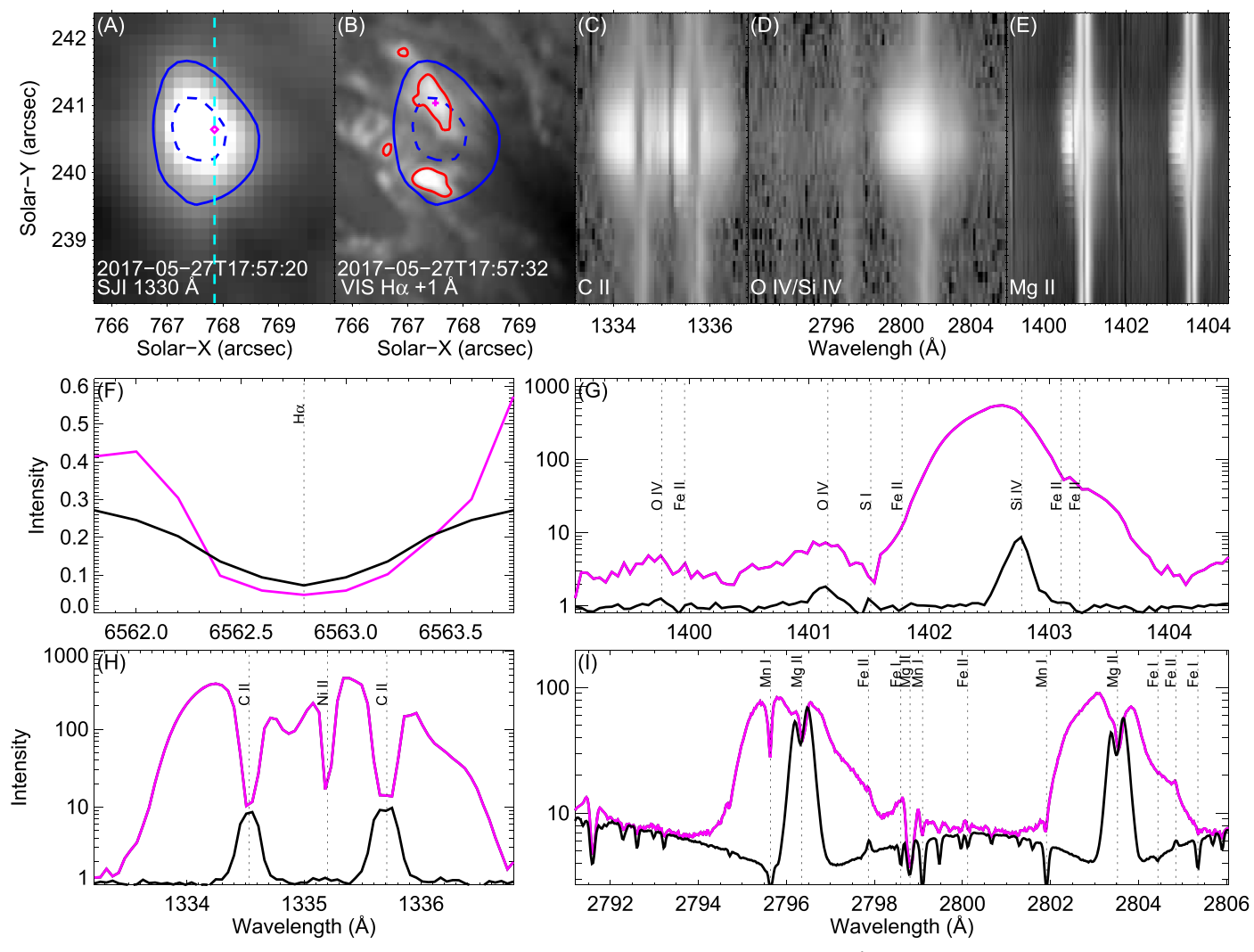


Figure 2. IRIS and GST observations of an EB-related UV burst and its corresponding EBs. (A): IRIS/SJI 1330 Å image taken at 17:57:20 UT on 2017 May 27. The cyan dashed line marks the IRIS slit position. (B): GST/VIS $H\alpha + 1$ Å image taken at 17:57:32 UT. The solid and dashed blue contours in (A) and (B) indicate the location of the UV burst identified using a threshold of 3σ and 5σ , respectively. The red contours in (B) mark the EB locations. (C)–(E): Simultaneously taken IRIS spectral images in three spectral windows. The intensities in (A)–(E) are shown in arbitrary units. (F): Normalized $H\alpha$ spectral profile (the purple line) at the location marked by the purple plus sign in (B). The black line represents the reference line profile. (G)–(I): IRIS spectra (purple lines, in the unit of countrate) at the location marked by the purple diamond in (A). The black lines represent the reference spectra from a plage region. The rest wavelengths of several spectral lines are marked by the vertical dashed lines in (F)–(I).

prominent dark flows in the $+1\,\text{Å}$ images appear to obscure some EB candidates. For this data set we lowered the threshold to 3σ , so that $\sim\!0.15\%$ pixels pass the thresholds for both data sets. We then examined the 11- or 5-point $H\alpha$ spectra of these EB candidates, and identified 161 EBs from the two data sets. In the meantime, we can see some transient compact brightenings from the *IRIS* 1330 and/or 1400 Å images. Similarly, we used a threshold of 3σ to identify UV bursts from the 1330 Å images taken on 2017 May 27. For the 2015 June 25 observation, we used a threshold of 2.5σ to identify UV bursts from the 1400 Å images. A similar approach has been suggested by Young et al. (2018). Twenty ($\sim\!12\%$) of the identified EBs appear to be associated with UV bursts. This fraction is not that different from the fractions found by Grubecka et al. (2016) and Tian et al. (2016).

Note that a more strict identification of UV bursts relies on an examination of the *IRIS* spectra. However, only a few compact brightenings in the TR images were scanned by the *IRIS* slit. An example is presented in Figure 2, where the slit

crosses a brightening in the IRIS/SJI 1330 Å image taken around 17:57:20 UT on 2017 May 27. We examined the IRIS spectra at the brightening, and found that the Si IV, C II, and Mg II line profiles are greatly enhanced and broadened. The absorption feature of Ni II 1335.20 Å is also obvious. Thus, this brightening is a typical UV burst (Peter et al. 2014; Young et al. 2018). We also notice the following characteristics for this UV burst: (1) the O IV 1401.156/1399.774 Å lines are very weak; (2) the Mg II k, h, and subordinate lines reveal a significant enhancement at the wings and no obvious enhancement in the cores; (3) the S I 1401.514 Å line is broadened with a central reversal. These properties are similar to those of EBrelated UV bursts (Tian et al. 2016). We can clearly see two EBs within the spatial range covered by this UV burst. The H α profile of the northern EB is presented in Figure 2(F), which shows an obvious enhancement at the wings and no enhancement at the core. The other EB has a similar $H\alpha$ profile. The UV burst appears to overlap more with the northern EB, which becomes evident if we increase the

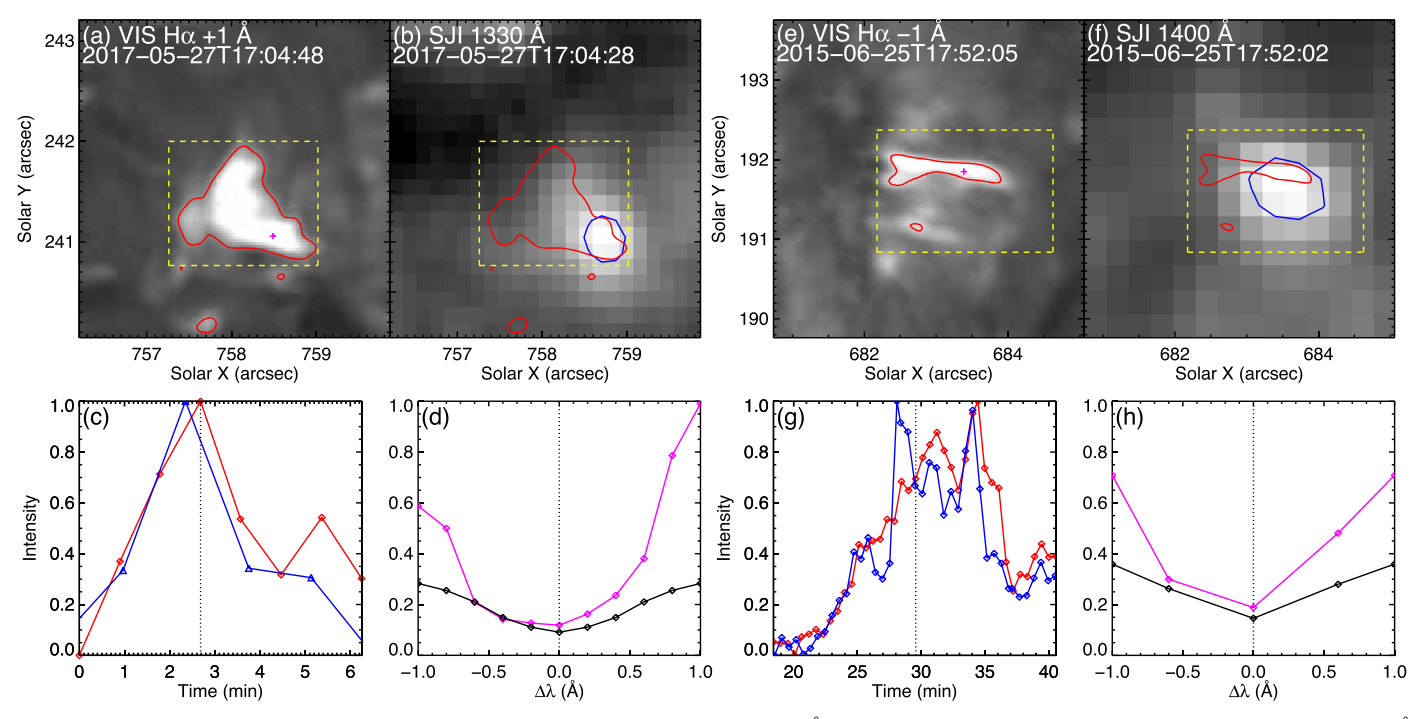


Figure 3. Two examples of flame-like EBs and associated UV bursts. (a): GST/VIS H α +1 Å image taken at 17:04:48 UT on 2017 May 27. (b): *IRIS*/SJI 1330 Å image taken at 17:04:28 UT. The blue contour marks the UV burst. The red contours in panels (a) and (b) outline the location of the EB. The intensities in (a) and (b) are shown in arbitrary units. (c) Temporal evolution of the total intensities of H α +1 Å (red) and SJI 1330 Å (blue) within the yellow box shown in (a) and (b). The vertical line indicates the time shown in (a). (d): The H α spectral profile (the purple line) at the location marked by the purple plus sign in (a). The reference profile is shown in black. The vertical line indicates the rest wavelength. The normalized intensities are shown in (c) and (d). (e)–(h): Same as (a)–(d) but for another event observed around 17:52:05 UT on 2015 June 25.

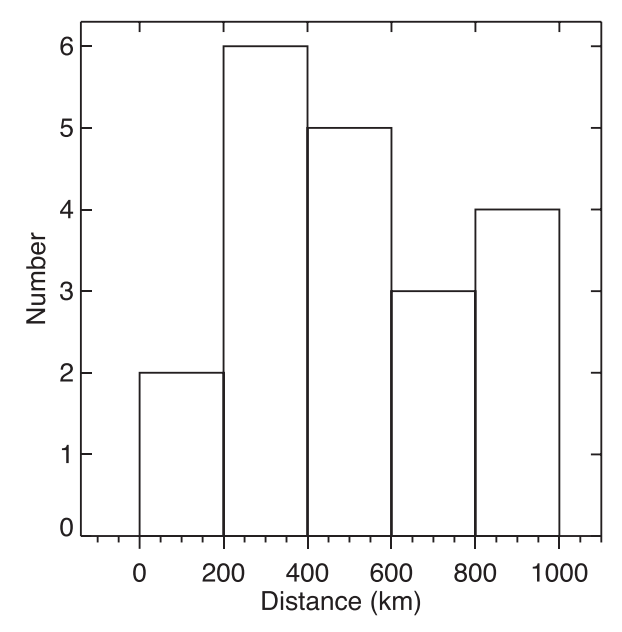


Figure 4. Histogram of the distance between the footpoint of an EB and the geometrical center of its associated UV burst.

threshold from 3σ to 5σ for UV burst identification. In addition, compared to the southern EB, the intensity variation of the northern EB shows a much higher correlation with that of the UV burst, suggesting that the UV burst is likely associated with the northern EB only. Another possibility is that these two EBs form at the footpoints of a chromospheric loop, all of which is heated during reconnection (Reid et al. 2015). In this case the two EBs should be located in magnetic field regions with

opposite polarities, which cannot be confirmed in this nearlimb observation. It is worth mentioning that the reference $H\alpha$ line profile (averaged over the whole FOV) is asymmetric, and the intensities at the blue wing are lower than those of the red wing. This asymmetry is not physical. To remove this instrumental effect, we have forced the reference profile to be symmetric by multiplying the intensity at each wavelength position at the blue wing by a factor. The line profile at each EB was then scaled using these factors at multiple wavelengths. Note that this asymmetry does not affect our EB identification, as only the relative changes of spectral intensities need to be considered.

Previous observations showed that most compact transient brightenings in SJI 1330/1400 Å images have significantly enhanced and broadened Si IV and C II line profiles (e.g., Tian et al. 2016; Chen et al. 2019). Thus, we treat all such brightenings that pass the thresholds mentioned above as UV bursts, though we could not examine the IRIS spectra of most brightenings due to the observational limitation. In total we have identified 61 UV bursts, and \sim 31% of them are connected to EBs. Figure 3 presents another two examples. The first event was observed on 2017 May 27. The intensities at the extended wings of H α are greatly enhanced, while the intensities near the $H\alpha$ core do not change too much. Obviously, this is a typical EB. The EB exhibits a flame-like morphology in the H α wing image, which is typical in near-limb observations (Hashimoto et al. 2010; Watanabe et al. 2011; Rouppe van der Voort et al. 2016). A visual inspection of the image sequence suggests that the UV burst is located at the top of the flame-like EB. Such a spatial offset likely reflects a height difference of the two phenomena. An earlier study by Vissers et al. (2015) also suggested that EBs are likely hotter in their tops. It is also

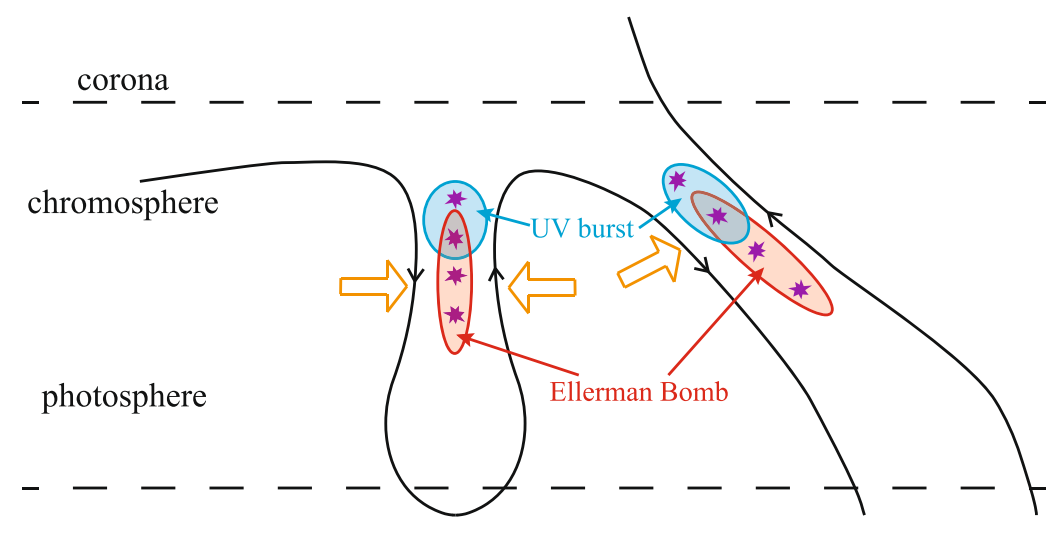


Figure 5. Cartoon showing a possible connection between some EBs and UV bursts. The black solid lines, red stars, and yellow arrows represent magnetic field lines, multiple X points within the current sheets, and the reconnection inflows, respectively.

interesting that the intensity variations of the EB and UV burst are very similar.

The second event presented in Figure 3 was observed on 2015 June 25. Although we could only obtain 5-point $H\alpha$ spectra, we can still see obvious enhancements only at the wings and not at the core, consistent with the definition of an EB. The EB also exhibits a flame-like morphology. Moreover, it reveals an inverted "Y"-shape structure at the footpoint, which is believed to result from magnetic reconnection between small magnetic bipoles and unipolar background fields (Shibata et al. 2007). Similar structures have also been identified from other high-resolution observations of EBs (Watanabe et al. 2011; Tian et al. 2016, 2018a). Similar to the first event, the associated UV burst is located at the top of the flame-like EB, and intensities of the EB and UV burst show correlated variations.

We have examined all of the 20 identified EBs that are associated with UV bursts, and found that the UV bursts indeed have a clear tendency to appear at the upper parts of the EBs. To quantify the spatial offset between an EB and its associated UV burst, we measured the distance between the footpoint of the EB and the geometrical center of the UV burst. The projected spatial offsets are generally a few hundred km (Figure 4), suggesting that UV bursts are formed at least a few hundred km higher compared to their associated EBs. We found that all the EB-related UV bursts and their associated EBs exhibit an obvious partial overlap in their locations, possibly indicating a partial overlap of their formation heights. But we cannot exclude the possibility that the overlap is caused by the projection effect.

In addition, we found that the intensities of 15 EB-related UV bursts and their associated EBs reveal a similar temporal evolution (correlation coefficient ≥0.7). The coherent evolution strongly suggests that these EBs and their associated UV bursts are caused or modulated by a common physical process. Calculations of the EB intensities in the other five events are affected by unrelated brightenings or flows, resulting in low correlations between the intensities of EBs and UV bursts in these events.

It has been suggested that UV bursts may be produced by reconnection processes that are dominated by the plasmoid instability (e.g., Innes et al. 2015; Ni et al. 2016). In the 2.5D

simulations of Nóbrega-Siverio et al. (2017) and Rouppe van der Voort et al. (2017), plasmoids are found in a wide range of atmospheric heights. In addition, recent models of Priest et al. (2018) and Syntelis et al. (2019) have shown that the plasma properties largely depend on the reconnection height. Inspired by our results and these models, we propose the following scenario (Figure 5) to explain the connection between some EBs and UV bursts: during flux emergence a nearly vertical current sheet may form and extend from the photosphere to the chromosphere. The current sheet could be located between the two sides of a U-loop produced through interaction between the emerging flux and convection, or at the interface between the emerging flux and an overlying field. As the current sheet becomes thinner, plasmoid instability is switched on. As a result, fast reconnection occurs and plasmoids are generated at different heights of the current sheet. Reconnections at chromospheric heights produce UV bursts, whereas lower-height reconnections within the same current sheet produce EBs. They may partially overlap in height. Such a scenario could explain the different temperatures of UV bursts and EBs, the spatial offset between them and their coherent intensity variations. Occasionally two EBs may occur close to each other simultaneously, as sketched in Figure 5. Then the associated UV bursts might merge to one larger event. This scenario would be consistent with the suggestion of Reid et al. (2015) and may explain the example shown in Figure 2. If the current sheet does not extend well above the TMR, we will only observe EBs. On the other hand, if reconnections occur only at greater heights, the resultant UV bursts will not be accompanied by EBs.

4. Summary

Using two coordinated near-limb observations between *IRIS* and GST, we have investigated the relationship between UV bursts and EBs. We have identified 161 EBs from the GST observations, with most of them exhibiting a flame-like morphology. About 20 EBs show signatures of UV bursts in the *IRIS* TR images.

The UV bursts often appear at the higher parts of flame-like EBs, indicating that UV bursts are likely formed a few hundred km above the TMR. At such heights the plasma density is

much lower than the photospheric density, and thus is more likely to be heated to $\sim \! 8 \times 10^4$ K. We have also found correlated variations of the intensities of most EBs and their associated UV bursts, suggesting a common cause or modulation of both phenomena.

To explain our observational results, we propose that an EB and its associated UV burst are produced by magnetic reconnection processes at the photospheric and chromospheric heights, respectively, within a roughly vertical current sheet.

This work is supported by NSFC grants 11825301, 11790304 (11790300), 41574166, 41774183, 41861134033, and U1731113, CAST innovation fund, the Max Planck Partner Group program, AFOSR FA9550-15-1-0322, and NSF AST-1614457 grants. BBSO operation is supported by NJIT, NSF AGS-1821294, and NSFC 11729301 grants. The GST operation is partly supported by the Korea Astronomy and Space Science Institute, Seoul National University, and the Strategic Priority Research Program of CAS with grant No. XDB09000000. *IRIS* is a NASA small explorer mission developed and operated by LMSAL with mission operations executed at NASA Ames Research center and major contributions to downlink communications funded by ESA and the Norwegian Space Centre. We thank Prof. Mingde Ding and Dr. Lei Ni for helpful discussions.

ORCID iDs

Hui Tian https://orcid.org/0000-0002-1369-1758
Tanmoy Samanta https://orcid.org/0000-0002-9667-6392
Haimin Wang https://orcid.org/0000-0002-5233-565X
Linghua Wang https://orcid.org/0000-0001-7309-4325
Jiansen He https://orcid.org/0000-0001-8179-417X

References

```
Bello González, N., Danilovic, S., & Kneer, F. 2013, A&A, 557, A102
Berlicki, A., & Heinzel, P. 2014, A&A, 567, A110
Cao, W., Gorceix, N., Coulter, R., et al. 2010, AN, 331, 636
Chen, Y., Tian, H., Zhu, X., et al. 2019, Science China Technological Sciences, in press
Chitta, L. P., Peter, H., Young, P. R., & Huang, Y.-M. 2017, A&A, 605, A49
Danilovic, S. 2017, A&A, 601, A122
De Pontieu, B., Title, A. M., Lemen, J. R., et al. 2014, SoPh, 289, 2733
Ding, M. D., Hénoux, J.-C., & Fang, C. 1998, A&A, 332, 761
```

```
Ellerman, F. 1917, ApJ, 46, 298
Fang, C., Hao, Q., Ding, M. D., & Li, Z. 2017, RAA, 17, 31
Fang, C., Tang, Y. H., Xu, Z., Ding, M. D., & Chen, P. F. 2006, ApJ,
Georgoulis, M. K., Rust, D. M., Bernasconi, P. N., & Schmieder, B. 2002, ApJ,
Grubecka, M., Schmieder, B., Berlicki, A., et al. 2016, A&A, 593, A32
Hansteen, V. H., Archontis, V., & Pereira, T. M. D. 2017, ApJ, 839, 2
Hashimoto, Y., Kitai, R., Ichimoto, K., et al. 2010, PASJ, 62, 879
Hong, J., Carlsson, M., & Ding, M. D. 2017a, ApJ, 845, 144
Hong, J., Ding, M. D., & Cao, W. 2017b, ApJ, 838, 101
Hong, J., Ding, M. D., Li, Y., Fang, C., & Cao, W. 2014, ApJ, 792, 13
Innes, D. E., Guo, L.-J., Huang, Y.-M., & Bhattacharjee, A. 2015, ApJ, 813, 86
Kim, Y.-H., Yurchyshyn, V., & Bong, S.-C. 2015, ApJ, 810, 38
Nelson, C. J., Freij, N., Reid, A., et al. 2017, ApJ, 845, 16
Nelson, C. J., Scullion, E. M., Doyle, J. G., Freij, N., & Erdélyi, R. 2015, ApJ,
  798, 19
Nelson, C. J., Shelyag, S., Mathioudakis, M., et al. 2013, ApJ, 779, 125
Ni, L., Lin, J., Roussev, I. I., & Schmieder, B. 2016, ApJ, 832, 195
Ni, L., Lukin, V. S., & Murphy, N. A. 2018a, ApJ, 868, 144
Ni, L., Lukin, V. S., Murph, N. A., & Lin, J. 2018b, ApJ, 852, 95
Nóbrega-Siverio, D., Martínez-Sykora, J., Moreno-Insertis, F. L., & Rouppe van
  der Voort, L. 2017, ApJ, 850, 153
Peter, H., Tian, H., Curdt, W., et al. 2014, Sci, 346, 1255726
Priest, E. R., Chitta, L. P., & Syntelis, P. 2018, ApJL, 862, L24
Reid, A., Mathioudakis, M., Kowalski, A., et al. 2017, ApJL, 835, L37
Reid, A., Mathioudakis, M., Scullion, E., et al. 2015, ApJ, 805, 64
Rezaei, R., & Beck, C. 2015, A&A, 582, A104
Rouppe van der Voort, L., De Pontieu, B., Scharmer, G. B., et al. 2017, ApJL,
  851. L6
Rouppe van der Voort, L. H. M., Rutten, R. J., & Vissers, G. J. M. 2016, A&A,
  592, A100
Rutten, R. J. 2016, A&A, 590, A124
Shibata, K., Nakamura, T., Matsumoto, T., Otsuji, K., & Okamoto, J. T. 2007,
   Sci. 318, 1591
Syntelis, P., Priest, E. R., & Chitta, L. P. 2019, ApJ, 872, 32
Tian, H., Xu, Z., He, J., & Madsen, C. 2016, ApJ, 824, 96
Tian, H., Yurchyshyn, V., Peter, H., et al. 2018a, ApJ, 854, 92
Tian, H., Zhu, X., Peter, H., et al. 2018b, ApJ, 854, 174
Toriumi, S., Katsukawa, Y., & Cheung, M. C. M. 2015, ApJ, 811, 137
Toriumi, S., Katsukawa, Y., & Cheung, M. C. M. 2017, ApJ, 836, 63
Vissers, G. J. M., Rouppe van der Voort, L. H. M., & Rutten, R. J. 2013, ApJ,
  774, 32
Vissers, G. J. M., Rouppe van der Voort, L. H. M., Rutten, R. J.,
  Carlsson, M., & De Pontieu, B. 2015, ApJ, 812, 11
Watanabe, H., Kitai, R., Okamoto, K., et al. 2008, ApJ, 684, 736
Watanabe, H., Vissers, G., Kitai, R., Rouppe van der Voort, L., & Rutten, R. J.
  2011, ApJ, 736, 71
Yang, H., Chae, J., Lim, E.-K., et al. 2013, SoPh, 288, 39
Young, P. R., Tian, H., Peter, H., et al. 2018, SSRv, 214, 120
Zhao, J., Schmieder, B., Li, H., et al. 2017, ApJ, 836, 52
```